Journal of Materials Chemistry A

PAPER

View Article Online
View Journal | View Issue

Check for updates

Cite this: J. Mater. Chem. A, 2019, 7, 26927

Effect of Cd on cation redistribution and order-disorder transition in $Cu_2(Zn,Cd)SnS_4$†

Shreyash Hadke, [abc] Wei Chen,[d] Joel Ming Rui Tan,[ae] Maxim Guc, [f] Victor Izquierdo-Roca,[f] Gian-Marco Rignanese, [d] Geoffroy Hautier [d] and Lydia Helena Wong *[abe]

Cation substitution has been extensively used to improve the fundamental optoelectronic properties and the photovoltaic performance of kesterite solar cells, and some of the most promising results have been obtained by substituting zinc with cadmium. Structurally, the positive effects of Cd have been attributed to the expected increase in the formation energy of defects such as Cu_{Zn} + Zn_{Cu} due to the larger ionic radius of Cd^{2+} as compared to Zn^{2+}. However, *ab initio* calculations using density functional theory (DFT) showed similar formation energies for Cu_{Zn} + Zn_{Cu} in Cu_2ZnSnS_4 and Cu_{Cd} + Cd_{Cu} in Cu_2CdSnS_4. Further, in this report, it is shown that Cd does not directly substitute the zinc lattice sites (2d Wyckoff positions) in the Cu_2ZnSnS_4 structure, but rather, a two-way cation restructuring due to the continuous transformation of the structure from kesterite to stannite leads to Cu replacing Zn, and Cd occupying the Cu sites (2a Wyckoff positions) in the partially Cd-substituted $Cu_2Zn_{1-x}Cd_xSnS_4$. Hence, the structural reasons for the beneficial effects of Cd need to be reinterpreted. Here, using computational model based on cluster expansion (fitted on DFT data), Monte-Carlo simulations, and differential scanning calorimetry, it is shown that Cu_2CdSnS_4 has less structural disorder than Cu_2ZnSnS_4 even if the thermodynamic point defect formation energy calculated using diluted point-defect models for disorder-inducing Cu_{Zn} + Zn_{Cu} and Cu_{Cd} + Cd_{Cu} defects in these two materials is predicted to be similar. This difference in the structural disorder is due to a sharp order-disorder transformation in Cu_2ZnSnS_4 at about 530 K, and a continuous order-disorder transformation in Cu_2CdSnS_4 throughout the range of processing temperatures.

Received 30th August 2019
Accepted 11th November 2019

DOI: 10.1039/c9ta09572a

rsc.li/materials-a

1. Introduction

The photovoltaic performance of copper zinc tin sulfo-selenide ($Cu_2ZnSn(S,Se)_4$), a promising candidate for low-cost thin-film solar cells, is currently limited by point defects.[1–3] Many of these point defects have a low formation energy, which is attributed to the similar ionic radii of Cu and Zn.[2,4] Various approaches have been employed to tackle the formation of point defects. Cation substitution – that is, the substitution of one of the cations in $Cu_2ZnSn(S,Se)_4$ with an isovalent cation – has recently shown promise in altering the point defect characteristics. The substitution of Zn with Cd has been especially promising,[5,6] with the highest reported efficiency of 11.5% for a partial substitution of Zn with Cd in copper zinc tin sulphide (Cu_2ZnSnS_4).[7] The rationale behind the introduction of Cd in the Cu_2ZnSnS_4 structure is that the larger ionic radius of Cd^{2+} as compared to Zn^{2+} would increase the formation energy of the Cu_{Zn} + Zn_{Cu} antisite defect. However, DFT calculations predict that the formation energy of $Cu_{Zn/Cd}$ + Zn/Cd_{Cu} is unaffected by the substitution of Zn with Cd.[8] Hence, the structural characteristics that lead to the improved performance are unclear. Moreover, a detailed structural characterization is still missing for the partially Cd substituted $Cu_2Zn_{1-x}Cd_xSnS_4$ absorbers at compositions where the high efficiency is obtained. One of the reasons for this is that neutron diffraction, which has been used extensively to study the structure of kesterite,[9,10] cannot be used for cadmium containing samples because of the high neutron absorption cross section of Cd. Hence, alternative approaches are needed to study the structure of $Cu_2Zn_{1-x}Cd_xSnS_4$.

In this paper, we study the structural characteristics of copper zinc cadmium tin sulphide ($Cu_2Zn_{1-x}Cd_xSnS_4$) using X-

[a]School of Materials Science and Engineering, Nanyang Technological University, 639798, Singapore. E-mail: lydiawong@ntu.edu.sg

[b]Energy Research Institute @ NTU (ERI@N), Nanyang Technological University, 637553, Singapore

[c]Interdisciplinary Graduate School, Nanyang Technological University, 637371, Singapore

[d]IMCN, Université Catholique de Louvain, B-1348 Louvain-la-Neuve, Belgium

[e]Campus of Research Excellence and Technological Enterprise (CREATE), Nanyang Technological University, 637553, Singapore

[f]Catalonia Institute for Energy Research (IREC), Jardin de les Dones de Negre 1, Barcelona, 08930, Spain

† Electronic supplementary information (ESI) available: (1) X-ray diffraction, (2) Raman spectroscopy, and (3) heat capacity. See DOI: 10.1039/c9ta09572a

ray diffraction (XRD), Raman spectroscopy, density functional theory (DFT) and differential scanning calorimetry (DSC). We show that the intuitively expected substitution of Zn with Cd on 2d Wyckoff sites does not occur in the Cu_2ZnSnS_4 structure, but rather, due to the continuous transformation of the structure from kesterite to stannite with increasing Cd substitution, Cd replaces Cu at 2a sites, while Cu moves to the Zn 2d positions. Using DFT and Monte-Carlo calculations supported by DSC experiments, we show that Cu_2CdSnS_4 can have less disorder inducing Cu_{Cd} + Cd_{Cu} antisite defects compared to the Cu_{Zn} + Zn_{Cu} defects in Cu_2ZnSnS_4, even if the formation energy of these defects calculated using dilute point-defect models is predicted to be similar.[8] Since these disorder-inducing defects are not expected to directly affect the optoelectronic properties, it is proposed that the reduced Cu_{Cd} + Cd_{Cu} antisites can destabilize other compensated deleterious defects containing Cu_{Cd}, such as $2Cu_{Cd}$ + Sn_{Cd}, thereby contributing to the improvement in optoelectronic properties.

2. Experimental methods

2.1. Deposition of $Cu_2(Zn,Cd)SnS_4$ thin films

The thin films were deposited by spin-coating a solution of copper acetate hydrate (0.52 mol L^{-1}), zinc acetate dihydrate and cadmium acetate dihydrate (0.33 mol L^{-1}), tin chloride dihydrate (0.27 mol L^{-1}), and thiourea (2.06 mol L^{-1}), at 4000 rpm on Mo-glass substrates. The spin-coating process was repeated 13 times, and the sample was annealed in air at 280 °C for 2 minutes after spin-coating. These films were then sulfurized at 580–600 °C for 40 minutes in Ar + S atmosphere and were cooled naturally in the furnace. The Cu/[Cd + Sn + Zn] ratio was 0.86 and Sn/[Cd + Zn] ratio was 0.8 for all the samples.

2.2. Experimental characterization

XRD measurements were performed using a Bruker D8 Advance system using a Cu Kα radiation source (40 kV, 40 mA) in the grazing incidence mode, with a grazing angle of 4°. The use of GIXRD makes the results less sensitive to texture effects, and hence, we did not perform pole figure measurements to determine the preferred orientation of the thin films before analysing the XRD data in Section 3.1. XRD simulations were performed using the software VESTA.[11] Raman and photoluminescence measurements were performed at room temperature on bare $Cu_2Zn_{1-x}Cd_xSnS_4$ absorbers with 633 nm laser excitation in a back-scattering configuration using iHR-320 monochromator coupled with a CCD and InGaAs detectors, and FHR-640 monochromator coupled with a CCD detector. All spectra were calibrated by imposing the position of the main peak of monocrystalline Si to 520 cm^{-1}. Differential scanning calorimetry (DSC) and thermogravimetric analysis (TGA) were performed using Labsys EVO 1150 from SETARAM Instrumentation, having a resolution of 0.2 μg and 10 μW, with a temperature accuracy of 1 °C. About 20 mg of powder samples for DSC-TGA were obtained by scraping sulfurized Cu_2ZnSnS_4 and Cu_2CdSnS_4 thin films. The samples are equilibrated at 30 °C for 10 min before heating to 350 °C at a rate of 3 °C min^{-1} under vacuum.

2.3. Computational details

To understand the order-disorder phase transition of Cu_2ZnSnS_4 and Cu_2CdSnS_4, we performed canonical Monte-Carlo (MC) simulations with effective cluster interactions (ECIs) obtained through cluster expansion (CE) using the CASM code.[12] The ECIs were obtained by fitting to the density functional theory (DFT) total energies within a ternary CE formula in which the cationic sites can be occupied by either Cu, Zn (Cd), or Sn for Cu_2ZnSnS_4 (Cu_2CdSnS_4). We considered pair interactions up to the fourth nearest neighbour (4NN) and triplet interactions up to the second nearest neighbour (2NN). For each material, about 700 stoichiometric supercells comprising up to 32 atoms were enumerated, for which the total energies were calculated with the Vienna *ab initio* package (VASP)[13–16] adopting the Perdew–Burke–Ernzerhof (PBE) exchange-correlation functional[17–20] and including a Hubbard U correction for the Cu-3d states (U = 6 eV).[21] We used a kinetic cut-off energy of 500 eV for the projector-augmented wave basis sets and k-point meshes corresponding to a density of 1600 k-points per atom in the first Brillouin zone. The atomic positions and lattice vectors were allowed to relax until the forces were converged within 20 meV $Å^{-1}$. Based on a genetic algorithm, the cluster expanded total energies achieve a 10-fold cross-validation score better than 10 meV per atom. The subsequent MC simulations were performed with a 30 × 30 × 30 supercell amounting to a total of 216 000 atoms, among which half of the sites were active. Each MC run at a given temperature comprised 20 000 equilibration passes followed by 50 000 production passes with a sampling interval of 10.

3. Results and discussion

3.1. X-ray diffraction

3.1.1. Structural differences between Cu_2ZnSnS_4 and Cu_2CdSnS_4. It is known that Cu_2ZnSnS_4 thin films crystallize in the kesterite-type structure, while Cu_2CdSnS_4 films crystallize in the stannite-type structure (Fig. 1).[22,23] Before studying the structural trends due to the partial substitution of Zn with Cd, we outline the differences between Cu_2ZnSnS_4 and Cu_2CdSnS_4: (i) the 2a sites in kesterite Cu_2ZnSnS_4 are occupied by Cu while the 2a sites in Cu_2CdSnS_4 are occupied by Cd, and (ii) the 2d sites in kesterite Cu_2ZnSnS_4 are occupied by Zn while the 4d sites in stannite Cu_2CdSnS_4 are occupied by Cu. There are three possible ways in which perfectly ordered kesterite Cu_2ZnSnS_4 can transform into perfectly ordered stannite Cu_2CdSnS_4 (Fig. 2).

i. Kesterite to stannite transformation at a particular Cd content. In this model, before the kesterite to stannite transformation, Cd replaces Zn in the 2d site in the kesterite structure, and after the transformation, Cd replaces Zn in 2a sites in the stannite structure. This model is shown in Fig. 2a, with an example of the transformation occurring at Cd/[Cd + Zn] = 0.40.

ii. Continuous transformation from kesterite to stannite with Cd partially occupying the 2a and 4d sites. In this model, the

 This journal is © The Royal Society of Chemistry 2019

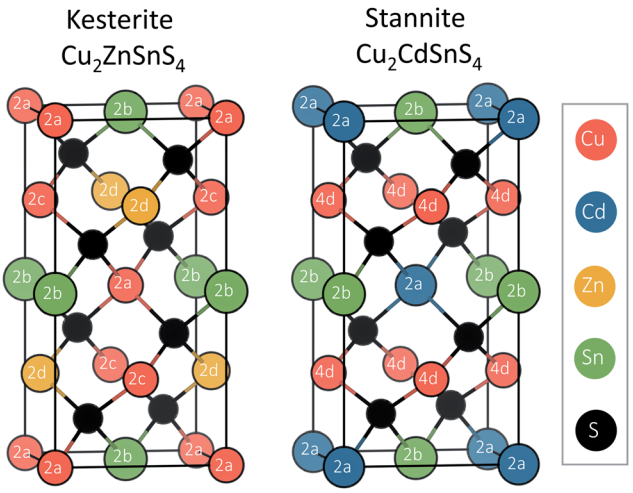

Fig. 1 Schematic of the crystal structures of Cu_2ZnSnS_4 and Cu_2CdSnS_4.

occupancy of the sites depends on the degree of transformation from kesterite to stannite, which depends on the Cd content. We assume a linear relationship between the degree of transformation and the Cd content. Hence, in this model, with increasing Cd content, Cu from the 2a site replaces Zn/Cd in the 4d sites (note that in the partially substituted $Cu_2Zn_{1-x}Cd_xSnS_4$, we use Wyckoff notations for stannite Cu_2CdSnS_4). The 2a sites left behind by Cu are occupied by Zn and Cd. This continues until all Zn are replaced with Cd, when all Cu from 2a sites go to 4d sites, and all 2a sites are occupied by Cd, that is, till we get the stannite Cu_2CdSnS_4 structure shown in Fig. 1.

iii. Continuous transformation from kesterite to stannite, with Cd occupying only the 2a sites. In this model, Cu from the 2a sites replaces Zn in the 4d sites. The 2a sites left behind by Cu are occupied by Cd, so that Cd and Zn are never present on the same Wyckoff sites.

In the sections below, these three models are referred to as model 1, model 2, and model 3, respectively. Having enumerated the possible models, we simulate the XRD patterns for these models at Cd/[Cd + Zn] = 0.0, 0.2, 0.4, 0.6, 0.8, and 1.0, and compare the simulated XRD patterns to the experimentally measured patterns for the same compositions.

3.1.2. Simulated and measured XRD patterns. We use the XRD data in the 2θ range 15–24 degrees to study the structure of $Cu_2Zn_{1-x}Cd_xSnS_4$ (Fig. 3; XRD patterns in the 2θ range 10–60 degrees shown in Fig. S1†). This narrow range is chosen because the 002, 101, and 110 peaks in this range are relatively insensitive to the change in c/a ratio of the tetragonal structure, while other strong XRD peaks are more sensitive to the c/a ratio than to the space group symmetry. Hence these peaks can reliably be used to differentiate between stannite and kesterite. The simulated XRD patterns for the three models show distinct trends.

For model 1 (Fig. 3a), before the kesterite to stannite transformation, the intensity of the 101 peak is significantly higher than that for peaks 002 and 110; after the transformation, the 101 peak can barely be observed. In Fig. 3a, although it is assumed that the transformation occurs for Cd/[Cd + Zn] > 0.4, the trend in the peak intensities observed above will remain the same irrespective of the Cd/[Cd + Zn] ratio. On the other hand, it can clearly be observed in the experimental XRD patterns

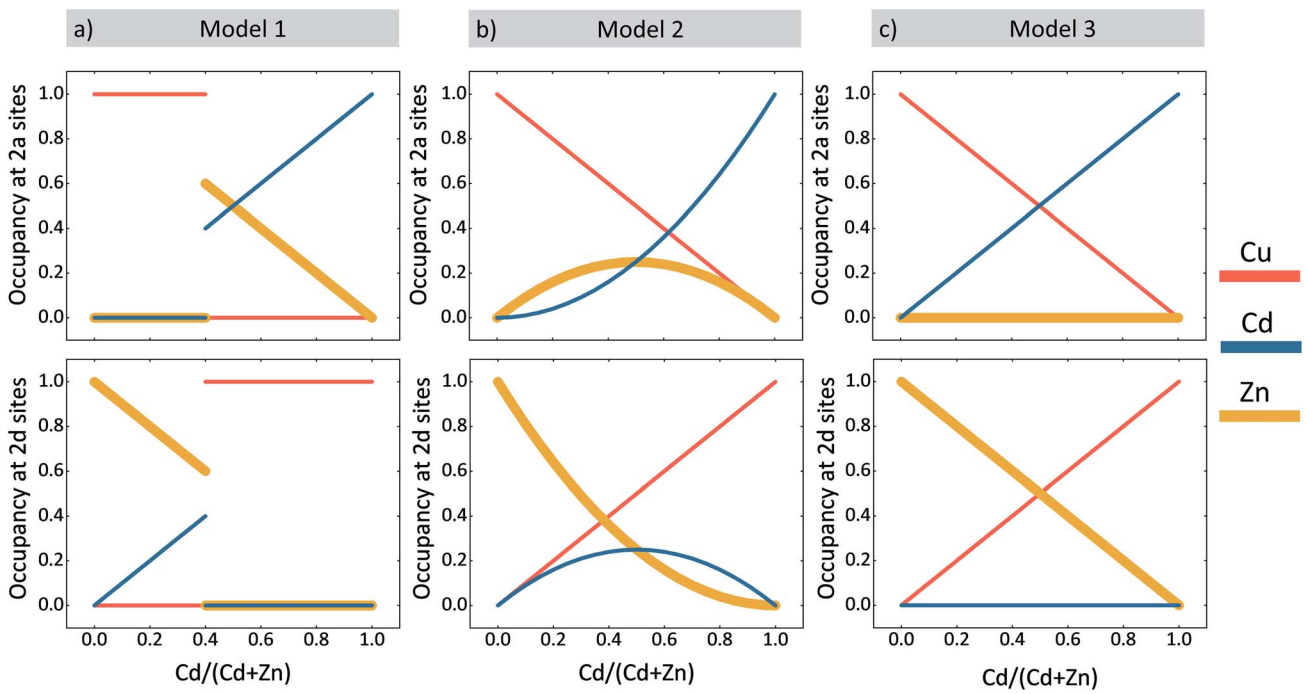

Fig. 2 Occupancy of 2a and 2d sites (corresponding to Wyckoff sites in kesterite structure) for the transformation of kesterite Cu_2ZnSnS_4 to stannite Cu_2CdSnS_4 in (a) model 1, (b) model 2, and (c) model 3.

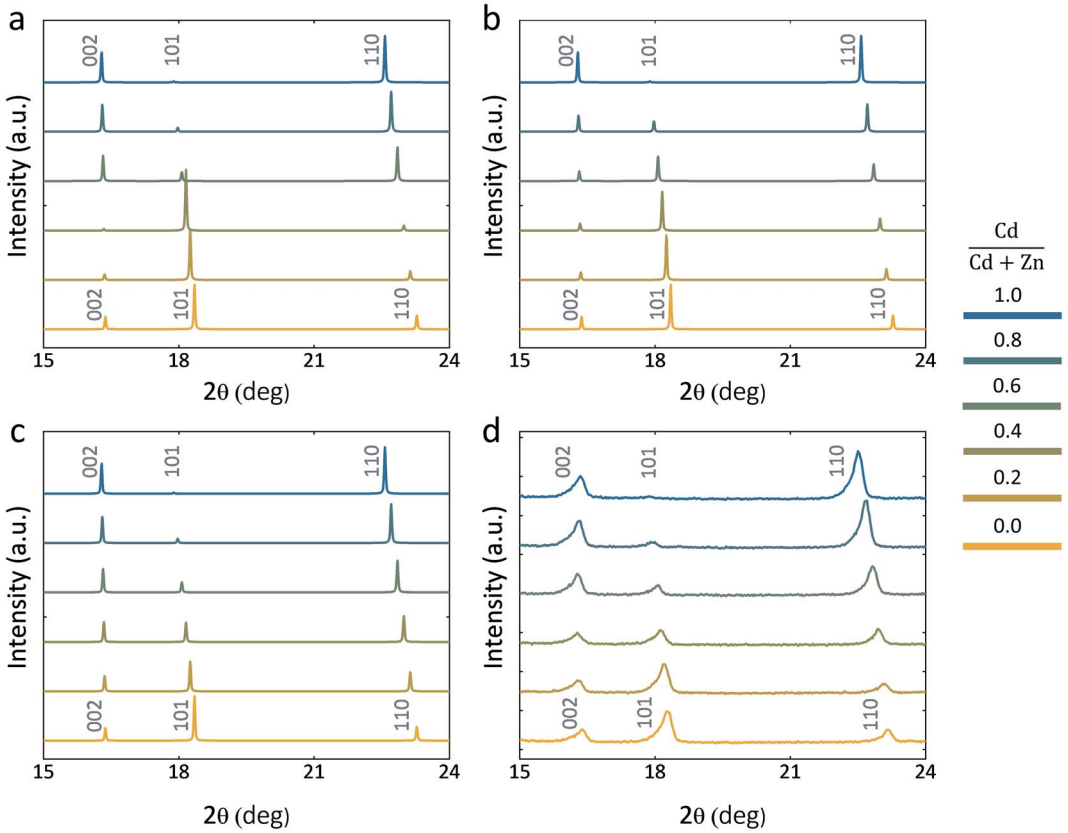

Fig. 3 Simulated XRD patterns at different Cu/[Cd + Zn] ratios for transformation of kesterite Cu_2ZnSnS_4 to stannite Cu_2CdSnS_4 according to (a) model 1, (b) model 2, (c) model 3, and the corresponding (d) experimental XRD patterns.

(Fig. 3d) that there is no drastic change in the peak intensities as expected in model 1. The change in the peak intensities in the experimental XRD patterns are gradual and span over the entire Cd/[Cd + Zn] range. Hence, we conclude that the kesterite to stannite transformation does not occur at any particular Cd/[Cd + Zn] ratio, but rather, is a continuous transformation, either according to model 2 or model 3.

For model 2 (Fig. 3b), the intensity of the 101 peak decreases gradually with increasing Cd/[Cd + Zn] ratio. This is consistent with the trend in the intensity of the 101 peak in the experimental XRD pattern (Fig. 3d). However, the relative intensities of the three peaks are not consistent with those observed in the experimental patterns. For example, in the simulated patterns, at Cd/[Cd + Zn] = 0.40, where the best photovoltaic performance is obtained,[22] the relative intensities of the three peaks are almost the same as those observed for Cd/[Cd + Zn] = 0. This is not observed in the experimental patterns, where the intensities of the three peaks at Cd/[Cd + Zn] = 0.4 are similar. The differences in the relative intensities of the peaks between the simulated and observed XRD patterns are even more significant for higher Cd/[Cd + Zn] ratios. At Cd/[Cd + Zn] = 0.60, the simulated patterns show a higher peak intensity for 101 peak as compared to 002 and 110 peaks, while the experimental patterns show an opposite trend – higher peak intensities for 002 and 110 compared to 101. Hence, based on comparisons of the relative intensities of the peaks, we conclude that the kesterite to stannite transformation does not follow model 2.

Finally, an excellent agreement is observed in peak positions, peak intensities, and relative peak intensities between the simulated XRD patterns for model 3 (Fig. 3c) and the experimentally observed patterns (Fig. 3d). Hence, we conclude that model 3 best describes the structural changes that occur as Zn is substituted with Cd. The continuous structural change from kesterite to stannite in this model is also supported by the evolution of peak positions in Raman spectra, that show a gradual change in the position of the main A/A_1 peak (Fig. S2†). In model 3 (Fig. 2c), the Cd that is 'substituting Zn' does not replace Zn at the 2d sites. Rather, Cu from 2a sites replaces Zn at 2d sites, and Cd occupies the 2a site left behind by Cu. Hence, the argument used to justify the substitution of Zn with Cd – that is, the difference in the ionic size – needs to be reinterpreted. In the following sections, we study the structural differences that could explain the optoelectronic effects of Cd substitution.

3.3. Cu–Zn and Cu–Cd disorder

3.3.1. Computational results. We used a model based on cluster expansion (fitted on DFT data) and Monte-Carlo (MC) simulations to evaluate how cation disorder depends on temperature in both Cu_2ZnSnS_4 and Cu_2CdSnS_4. The computed heat capacity of Cu_2ZnSnS_4 shows a sharp peak at 530 K

This journal is © The Royal Society of Chemistry 2019

(Fig. S3†), indicative of a second-order phase transition in agreement with previous computations[21,24] and Raman spectroscopy.[25] In contrast, such a second-order phase transition is not present for Cu_2CdSnS_4. Indeed, while Cu_2ZnSnS_4 undergoes phase transition from the ordered kesterite structure of the space group $I\bar{4}$ at low temperatures (Fig. 1) to the disordered structure of the space group $I\bar{4}2m$ at high temperatures,[21] for Cu_2CdSnS_4 the structural changes are absent since the ordered stannite structure already exhibits the space group $I\bar{4}2m$, thereby suppressing the order-disorder phase transition.

Fig. 4a shows the temperature dependence of the long-range order parameter (S), defined as $S = [P_{Cu}(Cu) - f(Cu)]/[1 - f(Cu)]$, where $P_{Cu}(Cu)$ is the occupancy of a Cu atom in the native Cu sites for the ordered structure, and $f(Cu)$ is the fraction of Cu atoms, which is equal to 2/3 as the Sn atoms are found immobile below 1200 K according to our MC simulations. The order parameter S ranges from 1 for an ordered structure to 0 for a fully disordered structure. For Cu_2ZnSnS_4, S decreases abruptly towards 0 above the critical temperature of ~530 K, as the Cu occupancy at the cationic sites approaches the random limit (Fig. 4b). Compared to Cu_2ZnSnS_4, the lack of a second-order phase transition leads to a less drastic decrease of S for Cu_2CdSnS_4. As a result, Cu_2CdSnS_4 is significantly more ordered (Fig. 4a and c) than Cu_2ZnSnS_4 for typical synthesis temperatures of 770–900 K (highlighted in grey in Fig. 4a–c).

3.3.2. Differential scanning calorimetry. To support the computational finding that Cu_2ZnSnS_4 undergoes an order-disorder phase transition and Cu_2CdSnS_4 does not, we performed differential scanning calorimetry measurements in conjunction with thermogravimetric analysis (DSC/TGA). In the case of Cu_2ZnSnS_4, we observe a peak in the heat flow at ~520 K (Fig. 4d), in remarkable agreement with the prediction of a sharp peak in the heat capacity for Cu_2ZnSnS_4 at ~530 K (Fig. S3†). Further, TGA curve for Cu_2ZnSnS_4 around this temperature shows no mass loss/gain, suggesting that the peak in the heat flow is due to the enthalpy of the order-disorder phase transformation.[26] In case of Cu_2CdSnS_4 a peak is observed at similar temperatures close to 520 K, although a clear weight change was also observed at this point, suggesting that this peak in the heat flow is not related to a phase transformation (Fig. 4e). Hence, we infer that the second-order phase transformation is suppressed in Cu_2CdSnS_4, in accordance with the theoretical predictions.

3.3.3. Implications of the order-disorder phase transition on Cu–Zn and Cu–Cd disorder. Regardless of the technique used for deposition of Cu, Zn, Sn, and S/Se on Mo-glass substrates, the absorbers for kesterite are annealed at a high temperature (770–900 K) in an S/Se atmosphere.[27] At these temperatures, there is a significant disorder present in $Cu_2ZnSn(S,Se)_4$. As the sample is cooled to room temperature, an order-disorder transformation takes place, as shown in Fig. 4b. If the transformation is not continuous – that is, the transformation occurs below a certain critical temperature – as in the case of Cu_2ZnSnS_4, then there needs to be a nucleation and growth process for the new phase. However, if the transformation is continuous – that is, the transformation occurs continuously as temperature is decreased – as in the case of

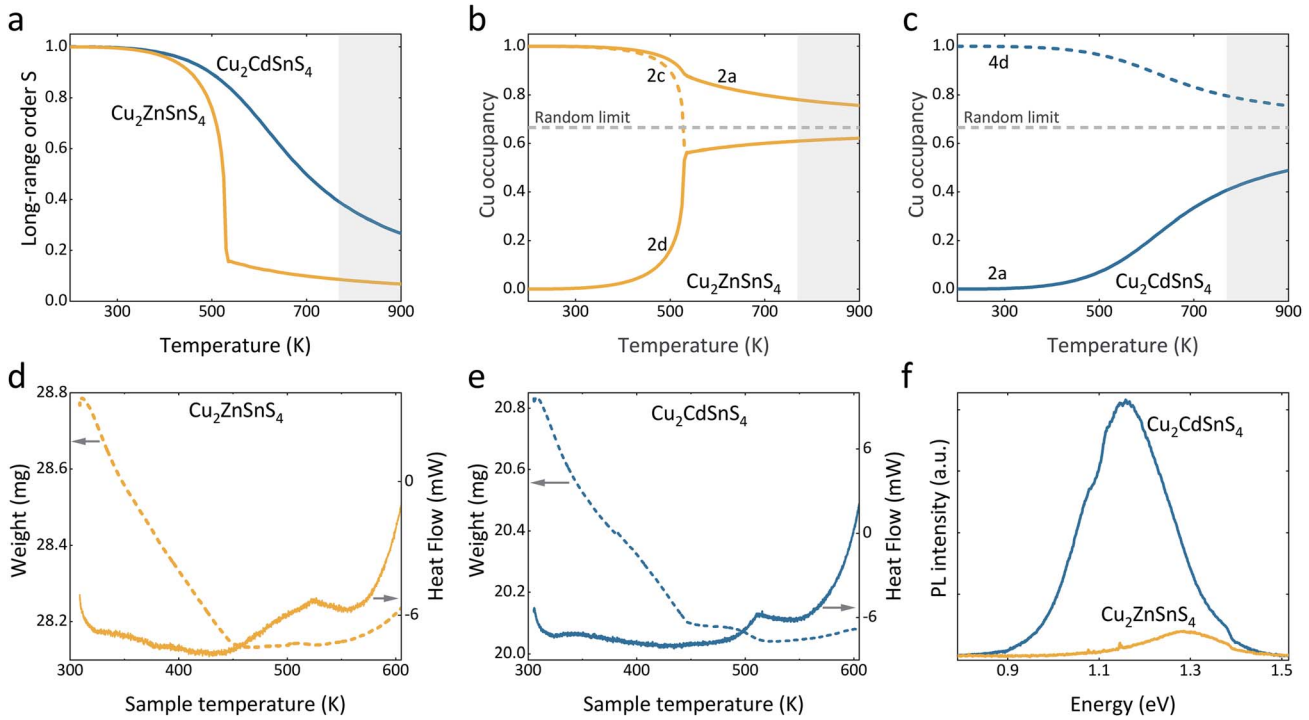

Fig. 4 (a) Long-range order parameter S and Cu occupancy at different Wyckoff sites in (b) kesterite $Cu_2ZnSnS4$ and (c) stannite Cu_2CdSnS_4 from Monte-Carlo simulations. Heat flow and weight from DSC/TGA experiments on (d) Cu_2ZnSnS_4 and (e) Cu_2CdSnS_4. (f) Photoluminescence data for Cu_2ZnSnS_4 and Cu_2CdSnS_4 under 633 nm laser excitation.

Cu_2CdSnS_4, then the need for the potentially kinetically slower nucleation and growth step is circumvented.

In the case of continuous transformation, the nucleation and growth steps are replaced by a continuous cation redistribution step, in which it is easier for kinetic reasons to equilibrate the system. Moreover, the ordering for Cu_2CdSnS_4 begins at high temperatures (that is, close to the sulfurization temperature of about 850 K) as soon as the sample is slowly cooled after sulfurization, while the ordering in Cu_2ZnSnS_4 only begins at low temperatures (that is, below the order-disorder transformation temperature of 530 K). Hence, the thermal energy available for the ordering process in Cu_2CdSnS_4 is larger than that available for Cu_2ZnSnS_4. Hence, under the same cooling rates, Cu_2CdSnS_4 would be more ordered than Cu_2ZnSnS_4.

We qualitatively explore the effect of structural disorder on optoelectronic properties of Cu_2ZnSnS_4 and Cu_2CdSnS_4 by comparing the photoluminescence characteristics. It has recently been suggested that $Cu_{Zn} + Zn_{Cu}$ disorder does not directly affect the optoelectronic performance[28] but can indirectly affect the more deleterious defects such as the $2Cu_{Zn} + Sn_{Zn}$, which can degrade the photovoltaic performance.[4,29] We hypothesize that the suppression of Cu_{Cd} due to the reduced $Cu_{Cd} + Cd_{Cu}$ disorder in Cu_2CdSnS_4 as compared to $Cu_{Zn} + Zn_{Cu}$ in Cu_2ZnSnS_4 could lead to enhanced suppression of Cu_{Cd} containing defect clusters such as $2Cu_{Cd} + Sn_{Cd}$ compared to $2Cu_{Zn} + Sn_{Zn}$. Since these defects are expected to affect the optoelectronic properties, we propose that the enhanced photoluminescence yield for Cu_2CdSnS_4 as compared to Cu_2ZnSnS_4 is partly due to the reduced $2Cu_{Zn/Cd} + Sn_{Zn/Cd}$ defects, which in turn are suppressed due to the reduced $Cu_{Cd} + Cd_{Cu}$ compared to $Cu_{Zn} + Zn_{Cu}$. However, it must be noted that Cd substitution itself directly affects the formation energy of $2Cu_{Zn/Cd} + Sn_{Zn/Cd}$, and suppresses these defects by increasing the formation energy of $2Cu_{Cd} + Sn_{Cd}$ in Cu_2CdSnS_4 compared to $2Cu_{Zn} + Sn_{Zn}$ in Cu_2ZnSnS_4.[8] Hence, the increased photoluminescence yield of Cu_2CdSnS_4 compared to Cu_2ZnSnS_4 could be a result of both the direct (Cd increasing the formation energy of $2Cu_{Cd} + Sn_{Cd}$) and indirect (Cd reducing the Cu_{Cd} disorder, thereby suppressing other Cu_{Cd} containing deleterious defects such as $2Cu_{Cd} + Sn_{Cd}$) mechanisms.

We note that the distinct behaviour of cation disorder in Cu_2CdSnS_4 in comparison to Cu_2ZnSnS_4 is not expected from earlier DFT calculations, which showed that the $Cu_{Cd} + Cd_{Cu}$ antisite pair has the same formation energy, and hence the same thermodynamic equilibrium concentration, as the $Cu_{Zn} + Zn_{Cu}$ pair in Cu_2ZnSnS_4.[8] Our MC simulations indicate that such studies based on diluted point-defect models may have difficulty in extrapolating to the correct description of cation disorder, in particular when phase transitions become relevant. In typical defect calculations, the isolated point defects were placed in an ordered system corresponding to the lowest-energy structure, thereby discarding collective interactions among defects and phase change. In the present case, the higher cation ordering of Cu_2CdSnS_4 is indeed driven by the absence of phase transition.

The study of order-disorder transformation using first-principles calculations and differential scanning calorimetry presented here can be used as a general strategy to predict the relative degree of disorder in complex multi-element compounds, and the XRD simulations combined with experimental data can be used to study the detailed structural characteristics without resorting to resource-expensive techniques such as neutron diffraction. Hence, the methods used in this report can be applied to screen emerging materials for applications where defects and disorder limit the desired optimal performance.

4. Conclusions

We studied structural effects of the substitution of Zn with Cd in Cu_2ZnSnS_4 to reveal a two-way cation redistribution as Cd is incorporated into the Cu_2ZnSnS_4 structure. We found that the intuitively expected substitution of Zn positions with Cd does not occur, but rather, Cd occupies the 2a sites – which are occupied by Cu in Cu_2ZnSnS_4 – and Cu from these sites replace Zn at 2d sites. Hence, the explanation hitherto used for the structural reasons that lead to improved performance of $Cu_2(Zn,Cd)SnS_4$ as compared to Cu_2ZnSnS_4 – that is, the increase in the formation energy of deleterious point defects due to the substitution of Zn with a larger Cd cation – need to be reinterpreted. Using MC simulations, we showed that Cu_2CdSnS_4 has more structural order compared to Cu_2ZnSnS_4, and that this can lead to improved optoelectronic properties even if the thermodynamic formation energy calculated using diluted point-defect models for disorder-inducing defects for Cu_2CdSnS_4 and Cu_2ZnSnS_4 is the same. We further proposed how this difference in structure affects the photoluminescence characteristics. Hence, we showed how the structural properties are correlated to the optoelectronic properties in this system, and we believe that the methods employed here can be used study other complex semiconductors.

Conflicts of interest

There are no conflicts to declare.

Acknowledgements

S. H., J. M. R. T., and L. W. acknowledge financial support from National Research Foundation (NRF), Singapore, through the Nanomaterials for Energy and Water Management (SHARE NEW) CREATE programme, MOE Tier 2 (MOE2016-T2-1-030S). W. C., G.-M. R., and G. H. acknowledge support from the F.R.S.-FNRS. W. C., G.-M. R., and G. H. acknowledge access to various computational resources: the Tier-1 supercomputer of the Fédération Wallonie-Bruxelles funded by the Walloon Region (grant agreement No. 1117545), and all the facilities provided by the Université catholique de Louvain (CISM/UCL) and by the Consortium des Équipements de Calcul Intensif en Fédération Wallonie Bruxelles (CÉCI). M. G. and V. I acknowledge support by the H2020 Programme under the project INFINITE-CELL (H2020-MSCA-RISE-2017-777968), by the

 This journal is © The Royal Society of Chemistry 2019

Spanish Ministry of Science, Innovation and Universities under the IGNITE (ENE2017-87671-C3-1-R), and by the European Regional Development Funds (ERDF, FEDER Programa Competitivitat de Catalunya 2007–2013). Authors from IREC belong to the SEMS (Solar Energy Materials and Systems) Consolidated Research Group of the "Generalitat de Catalunya" (Ref. 2017 SGR 862).

References

1 S. Giraldo, Z. Jehl, M. Placidi, V. Izquierdo-Roca, A. Perez-Rodriguez and E. Saucedo, *Adv. Mater.*, 2019, **31**, 1806692.
2 D. Shin, B. Saparov and D. B. Mitzi, *Adv. Energy Mater.*, 2017, **7**, 1602366.
3 A. Walsh, S. Chen, S.-H. Wei and X.-G. Gong, *Adv. Energy Mater.*, 2012, **2**, 400.
4 G. Rey, G. Larramona, S. Bourdais, C. Choné, B. Delatouche, A. Jacob, G. Dennler and S. Siebentritt, *Sol. Energy Mater. Sol. Cells*, 2018, **179**, 142.
5 S. H. Hadke, S. Levcenko, S. Lie, C. J. Hages, J. A. Márquez, T. Unold and L. H. Wong, *Adv. Energy Mater.*, 2018, **8**, 1802540.
6 Y. F. Tay, H. Kaneko, S. Y. Chiam, S. Lie, Q. Zheng, B. Wu, S. S. Hadke, Z. Su, P. S. Bassi, D. Bishop, T. C. Sum, T. Minegishi, J. Barber, K. Domen and L. H. Wong, *Joule*, 2018, **2**, 537.
7 C. Yan, K. Sun, J. Huang, S. Johnston, F. Liu, B. P. Veettil, K. Sun, A. Pu, F. Zhou, J. A. Stride, M. A. Green and X. Hao, *ACS Energy Lett.*, 2017, **2**, 930.
8 Z.-K. Yuan, S. Chen, H. Xiang, X.-G. Gong, A. Walsh, J.-S. Park, I. Repins and S.-H. Wei, *Adv. Funct. Mater.*, 2015, **25**, 6733.
9 G. Gurieva, L. E. Valle Rios, A. Franz, P. Whitfield and S. Schorr, *J. Appl. Phys.*, 2018, **123**, 161519.
10 S. Schorr, *Sol. Energy Mater. Sol. Cells*, 2011, **95**, 1482.
11 K. Momma and F. Izumi, *J. Appl. Crystallogr.*, 2011, **44**, 1272–1276.
12 J. C. Thomas and B. Puchala, *CASM 0.2.x*, https://github.com/prisms-center/CASMcode.
13 G. Kresse and J. Hafner, *Phys. Rev. B: Condens. Matter Mater. Phys.*, 1993, **47**, 558.
14 G. Kresse and J. Hafner, *Phys. Rev. B: Condens. Matter Mater. Phys.*, 1994, **49**, 14251.
15 G. Kresse and J. Furthmüller, *Phys. Rev. B: Condens. Matter Mater. Phys.*, 1996, **54**, 11169.
16 G. Kresse and J. Furthmüller, *Comput. Mater. Sci.*, 1996, **6**, 15.
17 J. C. Thomas and A. Van der Ven, *Phys. Rev. B*, 2013, **88**, 214111.
18 A. Van der Ven, J. C. Thomas, B. Puchala and A. R. Natarajan, *Annu. Rev. Mater. Res.*, 2018, **48**, 27.
19 B. Puchala and A. Van der Ven, *Phys. Rev. B: Condens. Matter Mater. Phys.*, 2013, **88**, 094108.
20 J. P. Perdew, K. Burke and M. Ernzerhof, *Phys. Rev. Lett.*, 1996, **77**, 3865.
21 S. P. Ramkumar, A. Miglio, M. J. van Setten, D. Waroquiers, G. Hautier and G. M. Rignanese, *Phys. Rev. Mater.*, 2018, **2**, 085403.
22 Z. Su, J. M. R. Tan, X. Li, X. Zeng, S. K. Batabyal and L. H. Wong, *Adv. Energy Mater.*, 2015, **5**, 1500682.
23 G. Sai Gautam, T. P. Senftle and E. A. Carter, *Chem. Mater.*, 2018, **30**, 4543.
24 K. Yu and E. A. Carter, *Chem. Mater.*, 2016, **28**, 864.
25 J. J. S. Scragg, L. Choubrac, A. Lafond, T. Ericson and C. Platzer-Björkman, *Appl. Phys. Lett.*, 2014, **104**, 041911.
26 F. Gascoin and A. Maignan, *Chem. Mater.*, 2011, **23**, 2510.
27 T. Ratz, G. Brammertz, R. Caballero, M. Leon, S. Canulescu, J. Schou, L. Gütay, D. Pareek, T. Taskesen and D.-H. Kim, *Journal of Physics: Energy*, 2019, **1**, 042003.
28 H. Hempel, R. Eichberger, I. Repins and T. Unold, *Thin Solid Films*, 2018, **666**, 40.
29 S. Chen, A. Walsh, X. G. Gong and S. H. Wei, *Adv. Mater.*, 2013, **25**, 1522.